JOURNAL OF GEOPHYSICAL RESEARCH, VOL. 113, E10005, doi:10.1029/2007JE003033, 2008

Horizontal structures and dynamics of Titan's thermosphere

I. C. F. Müller-Wodarg,[1] R. V. Yelle,[2] J. Cui,[2] and J. H. Waite[3]

Received 31 October 2007; revised 18 April 2008; accepted 4 June 2008; published 7 October 2008.

[1] The Cassini Ion Neutral Mass Spectrometer (INMS) measures densities of gases including N_2 and CH_4 in situ in Titan's upper atmosphere. We have used data from 13 targeted flybys of Titan (T5–T32) to construct an empirical model that describes the mean state of the thermosphere in the northern hemisphere, giving the N_2 and CH_4 densities between 1000 and 1600 km as a function of latitude and height. The principal features in the INMS data are well reproduced by this simple model. We find a pronounced oblateness in the thermosphere, with densities above 1100 km altitude increasing by around 70% from the northern (winter) pole to the equator, resulting in isobaric surfaces being ≃45 km higher over the equator than at the northern pole. Thermospheric temperatures derived from the densities tend to decrease with height from 149 ± 10 K to 140 ± 13 K near 1600 km. Considerable latitude differences are present in the temperatures below 1200 km. Near 1000 km altitude, temperatures reach 164 ± 6 K at 20°N and 131 ± 6 K near 80°N. Using our Thermosphere General Circulation Model with this thermal structure imposed, we derive thermospheric horizontal wind speeds reaching ∼150 m s^{-1}, with primarily poleward flow at equatorial latitudes which, northward of around 60°N, is accompanied by a band of prograde zonal winds of up to 50 m s^{-1}. At high latitudes, converging horizontal winds generate regions of strong subsistence. We find thermospheric dynamics to be sensitive to coupling from below. CH_4 abundances are enhanced in the northern polar region, which may result from transport by thermospheric winds.

Citation: Müller-Wodarg, I. C. F., R. V. Yelle, J. Cui, and J. H. Waite (2008), Horizontal structures and dynamics of Titan's thermosphere, *J. Geophys. Res.*, *113*, E10005, doi:10.1029/2007JE003033.

1. Introduction

[2] Before the arrival of Cassini/Huygens at the Saturnian system, the most detailed observations of Titan's thermosphere were made by the Voyager 1 Ultraviolet Spectrometer solar occultation experiment and dayglow measurements in November 1980 [*Broadfoot et al.*, 1981], yielding thermospheric densities of N_2, CH_4 and C_2H_2 in the morning and evening terminators at near-equatorial latitudes, from which exospheric temperatures of 196 ± 20 K and 176 ± 20 K were inferred, respectively [*Smith et al.*, 1982]. A comprehensive reanalysis of these data by *Vervack et al.* [2004] revised the original density values by *Smith et al.* [1982] and inferred lower temperatures of 153–158 K. On 14 January 2005, the Huygens probe descended through Titan's atmosphere, with its Atmospheric Structure Instrument (HASI) measuring total atmospheric density below 1400 km altitude by recording the deceleration of the probe by atmospheric drag. These measurements were carried out at near-equatorial latitudes, giving the first continuous profile of atmospheric density from the thermosphere to the troposphere of Titan. The derived pressure scale heights yielded atmospheric temperatures which in the thermosphere ranged from around 140–200 K, with strong oscillations of up to around 10 K amplitude around a mean temperature value of ∼175 K [*Fulchignoni et al.*, 2005]. In December 2004 the Cassini Ultraviolet Imaging Spectrometer (UVIS) observed two stellar occultations and derived vertical profiles of CH_4 and minor hydrocarbon species between around 450 and 1600 km altitude near latitudes of 36°S and 35–75°N [*Shemansky et al.*, 2005].

[3] On 26 October 2004, the Cassini spacecraft carried out its first in situ measurements of Titan's upper atmosphere down to a closest approach altitude of 1174 km. During this and the following targeted low-altitude flybys the Ion-Neutral Mass Spectrometer (INMS) instrument on board the spacecraft [*Waite et al.*, 2004] measured altitude profiles of neutral atmospheric constituents at an unprecedented level of detail, both in terms of species characteristics and spatial resolution. Analyses of the two earliest flybys inferred exospheric temperatures of 149 ± 3 K near 39°N at the evening terminator [*Waite et al.*, 2005; *Yelle et al.*, 2006] and between 154 and 162 K near 74°N close to midnight local time [*Müller-Wodarg et al.*, 2006; *De La Haye et al.*, 2007]. These early analyses of the INMS measurements suggested an unexpected trend of temper-

[1] Space and Atmospheric Physics Group, Imperial College London, London, UK.
[2] Lunar and Planetary Laboratory, University of Arizona, Tucson, Arizona, USA.
[3] Center for Excellence in Analytical Mass Spectrometry, Southwest Research Institute, San Antonio, Texas, USA.

0148-0227/08/2007JE003033$09.00

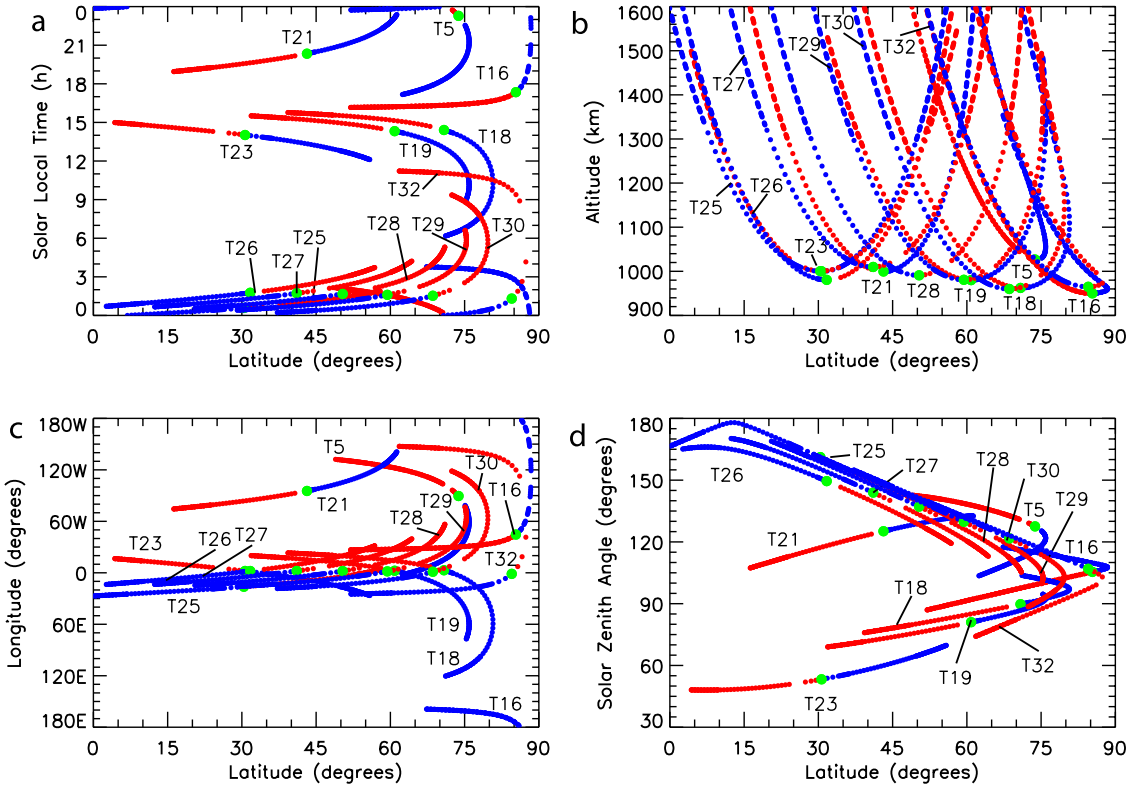

Figure 1. Trajectories of the Cassini spacecraft during targeted Titan flybys between 16 April 2005 (T5) and 13 June 2007 (T32). Only the paths of Cassini below 1600 km altitude are shown. Solid (blue) lines denote the inbound path, dashed (red) are outbound legs. The points of closest approach to Titan are marked with green/black dots. In order to illustrate the coverage of INMS observations used in this study, only the locations are marked where measurements were returned from by the INMS.

atures in Titan's thermosphere, with larger values in locations of lower solar EUV energy deposition. As pointed out by *Müller-Wodarg et al.* [2006], these analyses of density profiles from any single flyby were however potentially affected by horizontal structures in Titan's thermosphere, introducing an uncertainty in the temperature determination that could not be resolved with the available data sets.

[4] Between April 2005 and June 2007, the INMS measured thermospheric densities during 13 targeted flybys, a data set that allows for the first time a more comprehensive determination of horizontal structures on Titan. This study will present an analysis of the 13 INMS flybys from T5 to T32, constructing an empirical model that describes the latitude-height profiles of N_2 and CH_4 densities between 1000 and 1600 km altitude in Titan's northern hemisphere. We will use this information to constrain dynamics in the thermosphere with the ultimate aim of determining how winds affect the distribution of constituents such as CH_4. Section 2 describes the data reduction and empirical model; in section 3 we analyze the latitudinal structures of density and temperature. Sections 4 and 5 present calculations of thermospheric winds and investigate horizontal variations of CH_4 mole fractions. Our results are discussed in section 6.

2. Observations and Empirical Model

2.1. Titan Flyby Trajectories

[5] The INMS measurements used in this study were taken during 13 targeted Titan flybys which occurred between 16 April 2005 (T5) and 13 June 2007 (T32). Main characteristics of the flybys are shown in Figure 1 and listed in Table 1. All flybys considered here sampled only the northern hemisphere of Titan. Altitudes of closest approach (C/A) ranged from 950 km (T16) to 1025 km (T5), latitudes at C/A ranged from 30.36°N (T25) to 85.50°N (T16). As shown in Figure 1a, five of the closest approaches occurred in the daytime sector, but most solar zenith angles (Figure 1d) are larger than 90°, implying that the majority of measurements were taken during dusk or night conditions. Because of the uneven coverage of dayside and nightside passes, we will in this study not investigate local time changes in the thermosphere. Similarly, the majority of flybys occurred within the 60°E to 60°W longitude sector (Figure 1c), so we will not attempt to study longitude variations. No consistent trends with local time or longitude could be identified in the data set to date.

[6] Figure 1 illustrates the geographic coverage of INMS measurements considered in this study. At altitudes above around 1300 km most latitudes from the equator to around 80°N are well sampled, whereas below that height the regions equatorward of 15–20° are poorly sampled. In this study we consider only data taken below 1600 km altitude and will limit our discussions to the region from 20 to 80°N.

2.2. Empirical Model of Titan's Thermosphere

2.2.1. Construction of Model

[7] A major difficulty in deriving atmospheric properties from any single flyby is the fact that the spacecraft moves

Table 1. Summary of Titan Flybys Used in This Study[a]

Flyby Name	Flyby Date	C/A					F10.7 cm Flux at 1 AU	Titan-Saturn Angle (SLT)
		Altitude	Latitude	Longitude	LST	SZA		
T5	16 Apr 2005	1025	73.75	89.49	23.28	127.54	84	5.29
T16	22 Jul 2006	950	85.50	44.61	17.35	105.44	76	2.43
T18	23 Sep 2006	962	70.85	2.97	14.41	89.76	71	2.26
T19	9 Oct 2006	980	60.85	2.38	14.32	81.02	75	2.20
T21	12 Dec 2006	1000	43.30	95.38	20.34	125.19	99	2.03
T23	13 Jan 2007	1000	30.63	2.12	14.02	53.27	79	1.94
T25	22 Feb 2007	1000	30.36	−16.24	0.58	161.19	74	13.85
T26	10 Mar 2007	981	31.66	2.09	1.76	149.53	70	13.82
T27	25 Mar 2007	1010	41.08	2.13	1.72	143.96	73	13.72
T28	10 Apr 2007	991	50.36	2.03	1.67	137.16	69	13.73
T29	26 Apr 2007	981	59.39	1.65	1.60	129.79	81	13.66
T30	12 May 2007	960	68.58	1.23	1.53	121.73	71	13.64
T32	13 Jun 2007	965	84.52	−1.24	1.31	106.93	71	13.56

[a]Altitudes at closest approach (C/A) are given in km, latitude, longitude, and solar zenith angles (SZA) are given in degrees. Longitudes are defined as positive west. The local times of C/A are given in Titan local solar time (LST). The F10.7 cm solar flux is given in units of 10^{-22} W m^{-2}/Hz for 1 AU. The location of Titan around Saturn is given in hours of Saturn Local Time (SLT), where for 12.00 SLT Titan is positioned between Saturn and the Sun and for 0.00 SLT Titan is positioned on the antisunward side of Saturn.

both horizontally and vertically through Titan's atmosphere. Typically, the horizontal distance covered in Titan's atmosphere is at least a factor of 5 larger than the sampled height range. While density measurements from single flybys are often displayed as a function of altitude, it is dangerous to interpret such figures as height profiles because horizontal structures in the atmosphere also affect the measured profiles. In order to overcome this difficulty, we have used measurements from all flybys shown in Figure 1 to construct an empirical atmosphere model, allowing separation of the horizontal and vertical structures.

[8] The INMS measures the densities of N_2 and CH_4, but we use mass densities (ρ) and CH_4 mixing ratios ($\chi(CH_4)$) in order to construct the model and to derive the N_2 and CH_4 densities from them. This is done as mass density is the important quantity for hydrostatic equilibrium, an important constraint assumed in the model for ρ. In constructing the model we define an altitude grid from 1000 to 1600 km with a step size of 10 km and a latitude grid from 20 to 80°N with a step size of 2°. Since INMS measurement heights in most cases do not coincide with the initial chosen altitude levels, we carry out log linear interpolations in altitude of surrounding values of ρ and $\chi(CH_4)$ from relevant flybys on to the grid levels. Examples of resulting profiles are shown in Figures 2, 3, and 4 for altitudes 1030, 1200, and 1550 km, respectively. The values from individual flybys are plotted as a function of the latitude at which they were measured on the height level. In most cases both inbound and outbound values are available from each flyby, considerably improving the statistics.

[9] At each height level we fit the latitude variations with second-order Legendre polynomials, shown as dashed lines in Figures 2, 3, and 4. Since measurements are limited to the northern hemisphere, only symmetric Legendre functions P_0 and P_2 are used. We thus obtain at each altitude a set of Legendre polynomial amplitude values each for ρ and $\chi(CH_4)$. These amplitudes are plotted versus height in Figures 5 and 6. Figures 5a and 6a show the P_0 amplitudes, Figures 5b and 6b show amplitudes of P_2, plotted as fractions of P_0. Note that Legendre fits at each height are carried out independently, so the fact that consistent trends with altitude are visible in Figures 5 and 6 gives confidence in the values.

[10] In order to obtain a model that can be used for any arbitrary altitude, we fit altitude-dependent functions through the Legendre polynomial amplitudes, as shown in Figures 5 and 6. For P_0 amplitudes of ρ and $\chi(CH_4)$ we fit the logarithms with third-order polynomial functions of the form $P_0 = A + Bz + Cz^2 + Dz^3$, where z the altitude (in km). The vertical profiles of P_2/P_0 in ρ and $\chi(CH_4)$ were fit with a hyperbolical function of the form $x = A + (B - A) \cdot \tanh\{(z - C)/D\}$, where $x = P_2/P_0$. The values for coefficients A–D are given in Table 2. These sets of coefficients define a simple model for the N_2 and CH_4 densities in Titan's thermosphere. Since we used only INMS data from Titan's northern hemisphere in constraining the Legendre polynomials, the model should not be applied to the southern hemisphere without prior validation with measurements.

[11] It should be noted that in constructing the empirical model we assumed the atmosphere not to have changed significantly between the flybys. The data used in this study were taken over a period of around 2.5 years, which potentially allows changes in season, solar EUV radiation flux and magnetospheric forcing to be visible in Titan's thermosphere. Titan's solar declination angle changed from −23.34° (26 October 2004) to −12.71° (10 April 2007), so any seasonally induced variations will be smoothed in our model. To assess the variability of solar EUV flux, Table 1 lists the F10.7 cm flux (at 1 AU) for each flyby. The values show that we sampled Titan mostly at solar minimum conditions, at an average F10.7 cm flux value at 1 AU of 80×10^{-22} W m^{-2} Hz^{-1} with a standard deviation of 21%. The solar EUV fluctuations, therefore are small and likely to cause minor variations in Titan's thermosphere over the time span of the observations.

2.2.2. Atmospheric Variability and Model Uncertainties

[12] The empirical atmosphere model described in section 2.2.1 is an average representation of Titan's thermosphere as a function of altitude and latitude. We see in Figures 2, 3, and 4 the typical scatter of data points at different altitudes around the Legendre fit curves. Also shown in Figures 2–4 are the standard deviations, calculated from the differences between data points and the fitted functions. Figure 7 shows the standard deviations of mass density and CH_4 mixing ratio as a function of altitude. While mass density

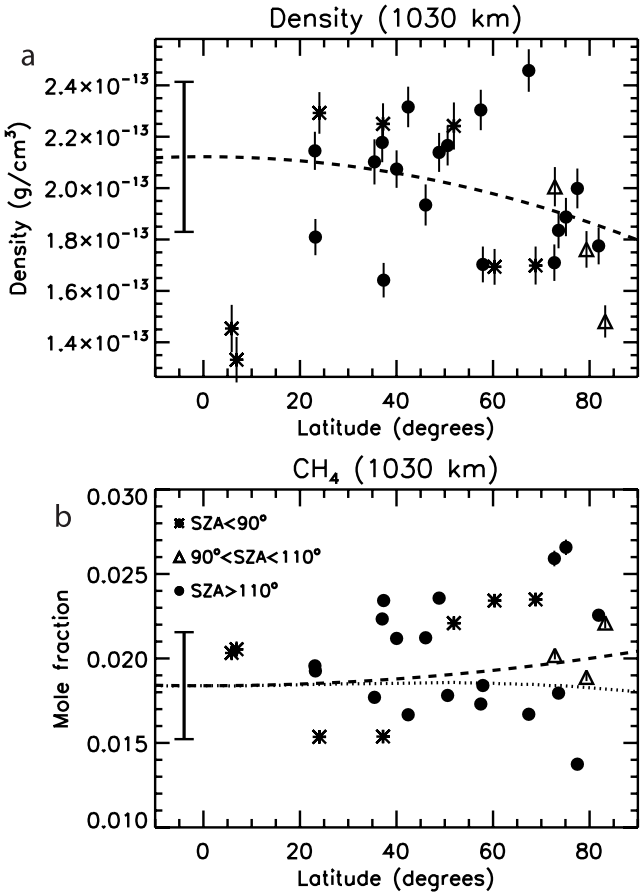

Figure 2. (a) Mass densities and (b) methane mixing ratios at 1030 km altitude, as observed by the INMS during multiple flybys (T5–T32) and plotted as a function of latitude. Best fits of Legendre polynomials, as used in the empirical atmosphere model, are shown as dashed lines. Since measurements from all available local times are plotted, markers of data points distinguish the solar zenith angles, with stars indicating sunlit conditions (SZA < 90°), triangles indicating dusk conditions (90° ≤ SZA < 110°) and solid circles indicating conditions of darkness (SZA ≥ 110°). Measurement error bars are superimposed but often too small to be visible. The standard deviations of data points around the fitted curves are shown in both Figures 2a and 2b. Dotted lines in Figure 2b are methane mole fractions on a level of constant pressure close to 1030 km determined by the empirical model, discussed in section 5.

uncertainties range from 10 to 50% between 1000 and 1600 km, those of CH_4 lie between 15 and 25%. Solid and dashed lines are third-degree polynomial fits to the standard deviations, with coefficients listed as $\sigma\rho$ and σ_{CH4} in Table 2.

[13] Two types of uncertainties affect the model, those inherent in the INMS measurements and those due to time and spatial variations in the atmosphere. Measurement errors by the INMS are due to counting statistics as well as overall calibration uncertainties and typically lie below 20%, implying that the standard deviations we find are due predominantly to local time, longitude or universal time variations not included in the model as well as other changes of the atmosphere, including possibly waves. As can be seen from Figures 2, 3, and 4, no systematic trend with solar zenith angle is apparent in the data, but this may in large part be due to the uneven statistics, with most measurements having been made at zenith angles larger than 110°. Similarly, longitude coverage of the measurements is, at present, insufficient to identify any longitudinal trends, which could result from standing waves or the magnetosphere interaction around Titan. As more measurements are made, future studies need to investigate these possible variations.

[14] Calculations by *Müller-Wodarg et al.* [2000], using a 3-D General Circulation Model (GCM) of Titan's thermosphere, found diurnal and hemispheric variability of up to 10–20 K in thermospheric temperatures resulting from solar EUV heating to be largest above 1300 km. This is consistent with our finding here that the standard deviations of ρ increase with altitude (Figure 7), so a large part of the spread may be due to diurnal changes in Titan's thermosphere driven by solar EUV heating on the dayside, but more data are needed to confirm this.

[15] The presence of strong waves in Titan's atmosphere is discussed by *Fulchignoni et al.* [2005] and *Müller-Wodarg et al.* [2006]. Amplitudes of pressure and density perturbations in the thermosphere reached around 4–12%, consistent with the standard deviation of measurements near 1000 km, but much smaller than those higher up. Waves such as those identified by *Müller-Wodarg et al.* [2006] may therefore only partly explain the variability we find here. It should be noted, though, that the P_2 amplitudes of $\chi(CH_4)$ in Figure 6 appear to contain wave-like variability with height, despite consisting of data sets scattered irregularly over time, which would be expected to 'wash out' many of the wave features.

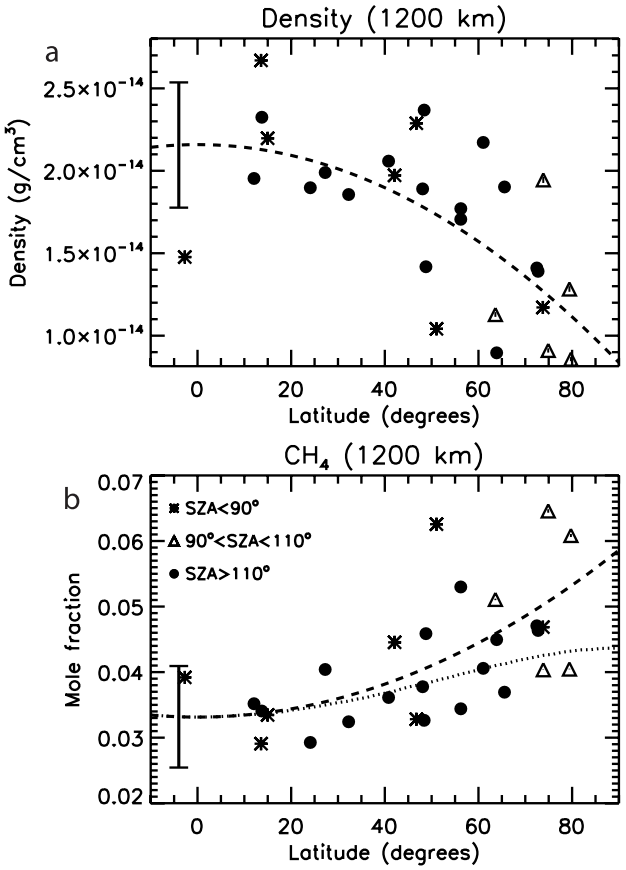

Figure 3. Same as Figure 2 but for an altitude of 1200 km.

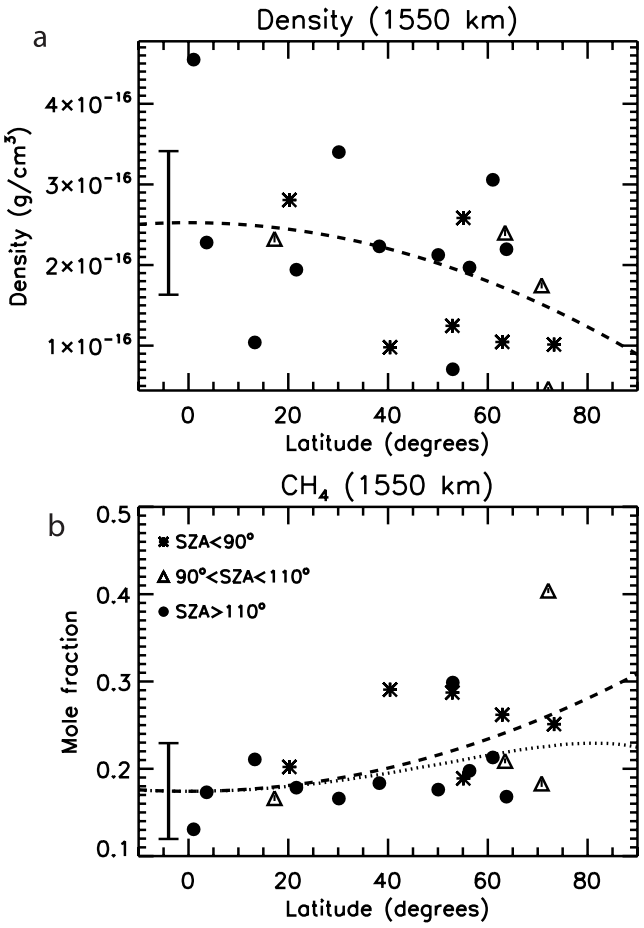

Figure 4. Same as Figure 2 but for an altitude of 1550 km.

[16] Variability in Titan's upper atmosphere may in part also be caused by changes in solar and magnetospheric forcing. In their calculations of Titan's thermal structure for solar minimum and maximum conditions, *Müller-Wodarg et al.* [2000] found that thermospheric temperature increased by up to 20 K at solar maximum. As seen in Table 1, the data we used in our study here were taken at low solar activity, making it unlikely that any of the variability we see in the data is linked to solar radiation forcing. More observations and comprehensive modeling are necessary to identify any magnetospheric forcing effects in Titan's upper atmosphere.

2.2.3. Validation of Model

[17] To validate the empirical model, Figures 8 and 9 show comparisons between modeled densities of N_2 and CH_4 (lines) and INMS observations (dots) for 6 representative flybys. Inbound values are shown in blue/black, outbound values in red/gray, model standard deviations are also shown for some altitudes. The modeled densities were extracted from the empirical model along the trajectories of T5, T19, T26 (Figure 8) and T18, T25, T32 (Figure 9). We chose the particular flybys of Figure 8 since they cover the widest combined range of latitude and altitude, as can be seen also from Figure 1. The flybys of Figure 9 as examples of poor matches between data and model.

[18] Overall, the match between the model and observations in Figure 8 is good. The difference between model and data is well within the model uncertainties, and the main features in the N_2 densities are reproduced. In particular, the difference between the inbound (blue/black) and outbound (red/gray) values at T19 are well captured by the model. This shows that many of the observed differences between inbound and outbound density profiles can be explained reasonably well by latitudinal variations in Titan's thermosphere. The average trends of CH_4 are reasonably well captured, but some of the differences between inbound and outbound profiles are not present in the model. The empirical model can be regarded as a reasonable representation of Titan's average thermospheric structure in the winter hemisphere at low solar activity.

[19] While the empirical model agrees reasonably well with measurements at most flybys, there are considerable differences at T18, T25 and T32, shown in Figure 9. Interestingly, the T25 flyby had a trajectory very similar to that of T26 through Titan's atmosphere, but the measured densities differ considerably. Near 1500 km altitude N_2 densities are $[N_2] \sim 7.1 \times 10^6$ cm^{-3} (T26) and $[N_2] \sim 1.7 \times 10^7$ cm^{-3} (T25), roughly a factor of 2 larger at T25. Corresponding CH_4 mixing ratios at that height are 18% (T26) and 15% (T25). The cause of this discrepancy is not certain but the similarity in geometry strongly suggests

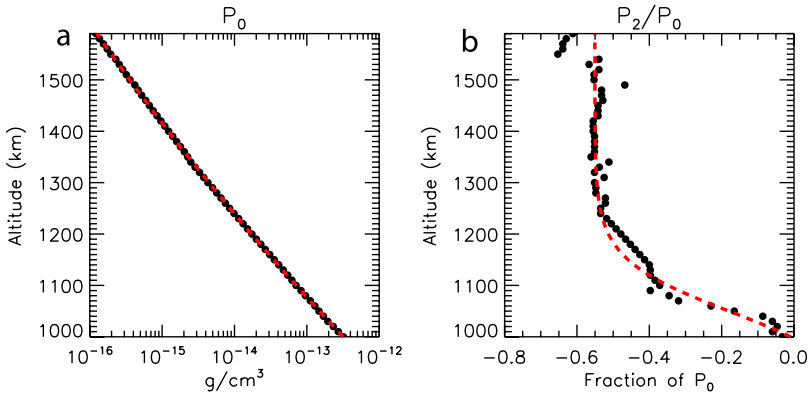

Figure 5. Amplitudes of the first two symmetric Legendre polynomials that best fit mass density in Titan's atmosphere observed by INMS. Examples of Legendre polynomial fits are shown in Figures 2, 3, and 4. (a) Amplitudes of P_0 (in g cm^{-3}) and (b) amplitudes of the ratio P_2/P_0. Also shown as dashed lines are the best fits to the points, using function coefficients given in Table 2 and described further in the text.

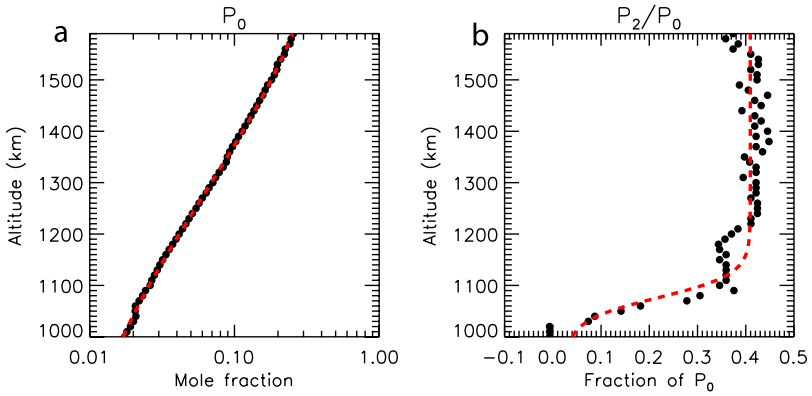

Figure 6. Same as Figure 5 but for CH_4 mixing ratios.

that it must be a temporal variation in the atmosphere. However, as seen from Table 1, the solar F10.7 cm flux was very similar during both flybys (74 and 70 $\times$ 10^{-22} W m^{-2} Hz^{-1}). In addition, Titan was at an almost identical location around Saturn during T25 and T26 (SLT = 13.85 and 13.82, respectively).

[20] While we find large discrepancies between the empirical model and INMS data during T18, T25 and T32 in terms of total densities (see Figure 9), the differences between inbound and outbound N_2 and CH_4 densities at T18 and T25 are well captured by the model. There appears to be no systematic difference between model and data: at T25 the model underestimates densities while at T18 and T32 it overestimates them.

[21] The overall conclusion we can reach from this is that Titan's atmosphere shows considerable variability with time. Examples such as flybys T25 and T26, which should give virtually identical results, differed considerably in the data. In Figures 2–4 we showed considerable scatter of the densities observed by INMS. Whether this variability is a signature of waves in the atmosphere or forcing from outside or a combination of both cannot be determined at this stage. Our empirical atmosphere model represents one state of the atmosphere, but one has to keep in mind the potential variations of the real atmosphere around this mean state described by our model.

3. Latitudinal Structures in Titan's Thermosphere

3.1. Mass Densities

[22] The empirical model allows us to quantify latitudinal structures of density in Titan's thermosphere. Figure 10 shows vertical and latitudinal profiles of mass density. The vertical density profiles (Figure 10a) are shown for latitudes 20°N (solid), 50°N (dash-dotted) and 70°N (dashed) between altitudes 1000 and 1600 km. Figure 10b shows normalized densities as a function of latitude at heights 1000 km (solid), 1050 km (dash-triple-dotted) and 1150 km (dashed). At 1000 km the latitudinal density variations negligible, while a distinctive latitude shape evolves at higher altitudes. Near 1050 km densities at 20°N are roughly 20% larger than those near 80°N. This latitudinal difference increases to around 70% above 1150 km and remains unchanged up to the upper boundary of our range. Model uncertainties between 1150 and 1590 km range from ~20 to 50% (see the error bars and Figure 7), so the latitudinal structures above 1150 km are larger than the model uncertainties.

[23] The mass density profiles of our empirical model show an oblateness to be present in Titan's thermosphere, clearly dominating the horizontal variations detected by INMS. Using observations only from the TA and T5 flybys, *Müller-Wodarg et al.* [2006] inferred the presence of this bulge, but derived a factor of 3 decrease in density from 30°N to 70°N, around 4 times more pronounced than we found in this study. Given an unresolved calibration issue with the INMS TA data which resulted in anomalously high densities and given the improved statistics of this study and the uncertainties in separating horizontal variations from vertical variations in the study by *Müller-Wodarg et al.* [2006], we expect our new value to be more reliable. However, a contributing factor to the smaller bulge found in this study may be time variations in Titan's thermosphere, given that the bulk of data used in this study were taken more than 1 year after those used by *Müller-Wodarg et al.* [2006] (see Table 1).

Table 2. Coefficients Describing the Vertical Change of Amplitudes of Legendre Polynomials P_0 and P_2 in Titan's Thermosphere Between 1000 and 1600 km Altitude as Well as Standard Deviations[a]

	A	B	C	D
ρ (P_0)	−9.12874	−0.0245442	5.46155×10^{-6}	-5.65851×10^{-10}
ρ (P_2/P_0)	−0.17415027	−0.55051365	1048.4497	102.84604
$\sigma\rho$	3.11710	−0.00766255	6.20478×10^{-6}	-1.52689×10^{-9}
$\chi(CH_4)$ (P_0)	3.33629	−0.0246300	2.33058×10^{-5}	-6.08782×10^{-9}
$\chi(CH_4)$ (P_2/P_0)	0.21880656	0.40943727	1076.2867	45.036168
σ_{CH4}	3.58841	−0.00797716	6.03850×10^{-6}	-1.47126×10^{-9}

[a]For ρ (P_0), $\chi(CH_4)$ (P_0) and standard deviations (σ) the coefficients A–D are for a third order polynomial of the form $x = A + B\,y + C\,y^2 + D\,y^3$, where x is the respective quantity and y is the altitude (in km). For ρ (P_2/P_0) and $\chi(CH_4)$ (P_2/P_0), coefficients A–D are for a hyperbolical function of the form $x = A + (B - A) \cdot \tanh\,(y - C)/D$, where x is again the respective quantity and y is the altitude (in km). The fits resulting from these coefficients are shown in Figures 5 and 6 as dashed lines. Standard deviations are given as fractions of background values and are plotted in Figure 7 (as percentages).

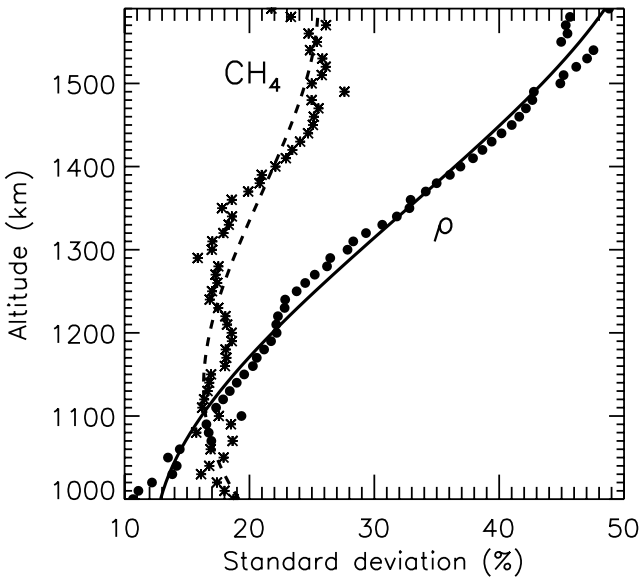

Figure 7. Standard deviations of CH_4 mixing ratios (stars) and mass density (dots) as a function of altitude. The values are fluctuations of measurements around the fitted Legendre polynomial curves, also shown in Figures 2, 3, and 4 as error bars. Dashed and solid lines are polynomial fits through the values, with coefficients given in Table 2. Standard deviations are given as percentages of the average background values.

[24] The Huygens Atmospheric Structure Instrument (HASI) measured decelerations of the probe during its descent through Titan's themosphere on 14 January 2005, from which mass densities have been inferred [*Fulchignoni et al.*, 2005]. The Huygens probe flew through thermospheric heights at equatorial latitudes of 9°S. We find for the equatorial latitude of HASI observations that our densities at 1000 km altitude are 2.4 times smaller than the HASI values, while at the upper boundary of HASI observations (1380 km) our densities are 4.9 times smaller. This comparison is valid for latitudes within around 20° of the equator, so any latitudinal motion of the probe along its descent trajectory will not affect the comparison. This systematic offset of the INMS data relative to the HASI values is as yet not understood. The Cassini Attitude and Articulation Control Subsystem (AACS) measures the torque on the spacecraft as it enters Titan's upper atmosphere on each flyby, providing an additional independent measurement of total density. Comparison of AACS-derived densities at 1000 km and those from the INMS show INMS densities to be smaller by an average factor of 2.6 than those from the AACS, very similar to the discrepancy factor between HASI and INMS at that altitude. The Pioneer Venus Orbiter Neutral Mass Spectrometer (PV-ONMS) similarly found an average offset factor of 1.6 that was needed to match densities in Venus' thermosphere with those measured by the descent probes and orbiter drag experiment and is not understood [*Hedin et al.*, 1983]. While

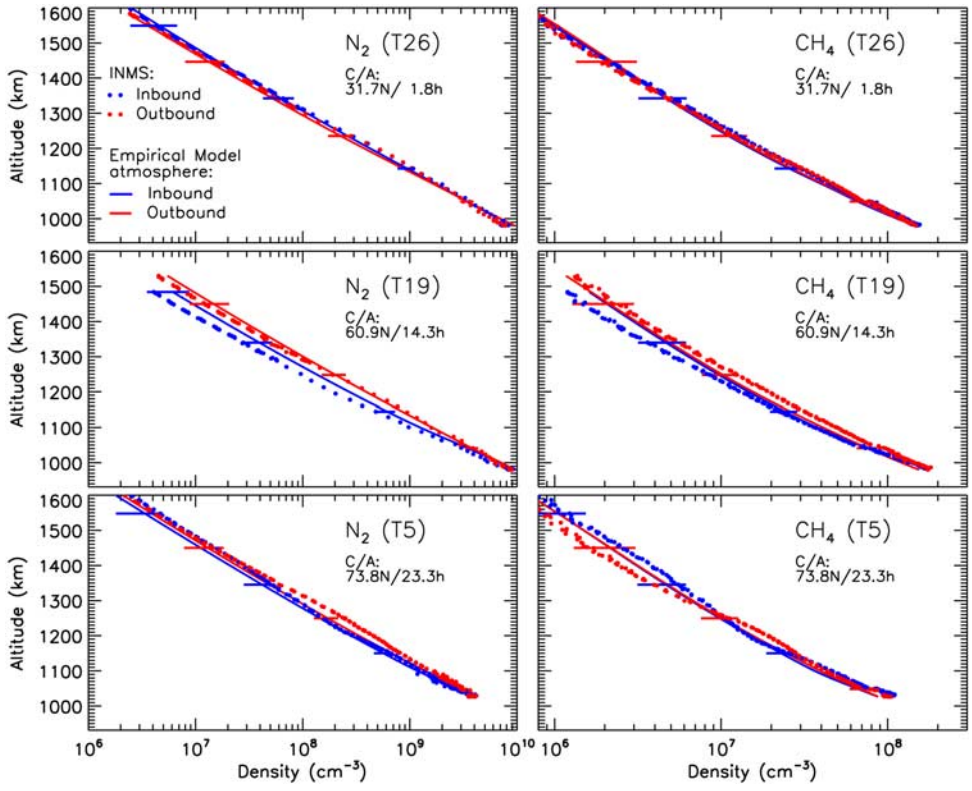

Figure 8. Examples of comparisons between our empirical model and densities of N_2 and CH_4 observed by INMS in Titan's upper atmosphere during flybys (a) T26, (b) T19, and (c) T5. Dots are the measurements and solid lines denote model values. Blue lines/markers are for the inbound trajectory legs, red lines/markers are along the outbound trajectory. Also shown are uncertainty error bars on the model profiles.

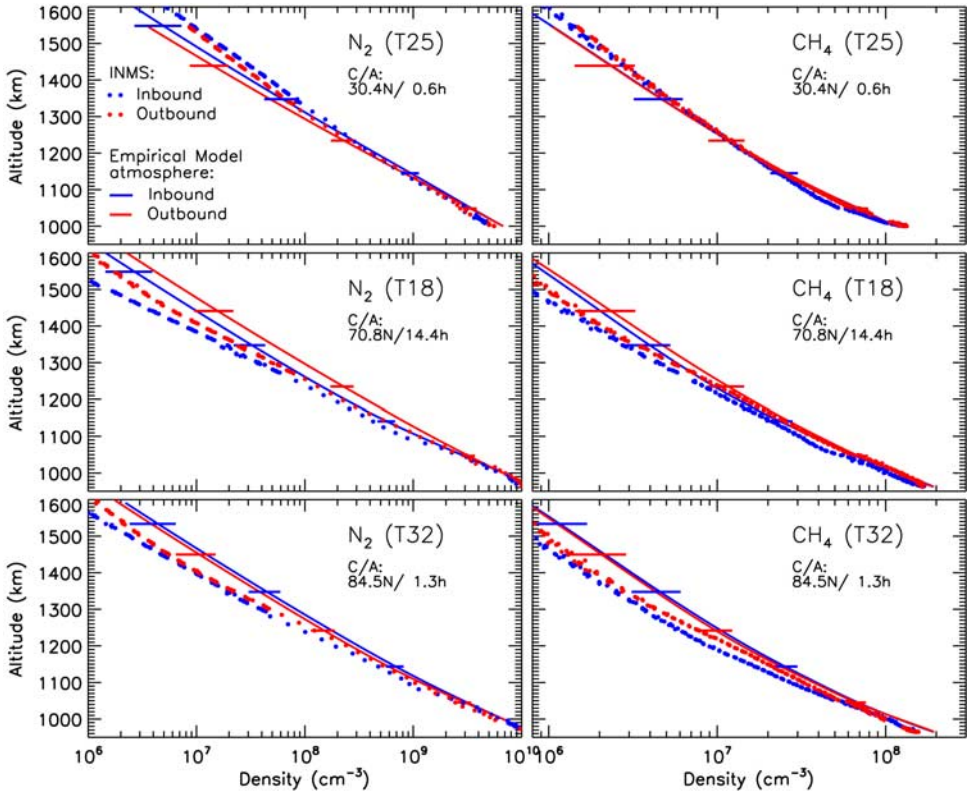

Figure 9. Same as Figure 8 but for flybys (a) T25, (b) T18, and (c) T32.

an uncertainty remains as far as the absolute calibration of the INMS densities is concerned, this does not affect the scientific conclusions of this study, in particular the horizontal structures, temperatures and dynamics but will ultimately affect the mapping of pressure levels and altitudes.

3.2. Temperatures

[25] Temperatures are not measured directly in Titan's thermosphere, but can be derived from the INMS density measurements. The procedure consists of first deriving vertical profiles of atmospheric pressure followed by calculations of temperatures from the ideal gas law, using the calculated pressure and measured density. Pressures are calculated by integrating the weight of the atmosphere from the top down [*Müller-Wodarg et al.*, 2006]. An upper boundary condition is needed for the temperature determination. We calculated this by evaluating the average density scale height between 1500 and 1600 km at each latitude. As shown by *Müller-Wodarg et al.* [2006], temperatures below around 1400 km depend very little on the choice of

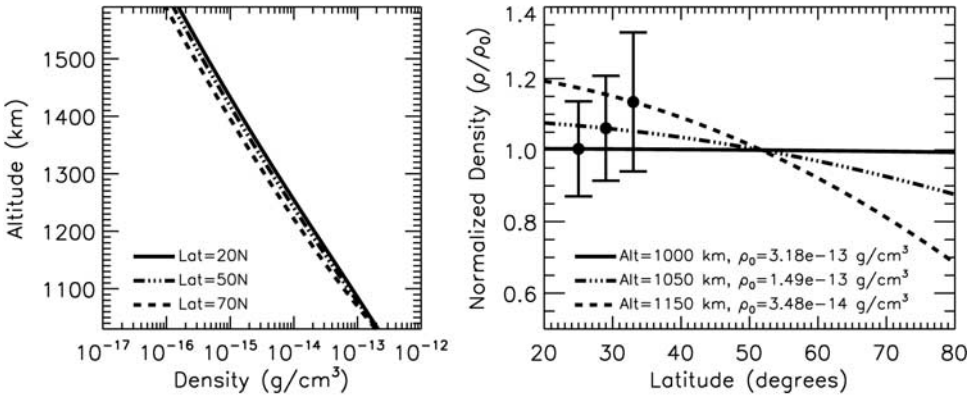

Figure 10. Mass densities in Titan's thermosphere, as given by our empirical model. (a) Vertical profiles at latitudes 20°N (solid), 50°N (dash-dotted) and 70°N (dashed), illustrating the change with altitude of latitudinal variations. (b) Densities at fixed altitudes of 1000 km (solid), 1050 km (dash-dotted) and 1150 km (dashed), normalized to their average values at each height. The latitudinal density structure is roughly uniform above 1100 km, as can be seen also in Figure 10a. Standard deviations of densities are also shown.

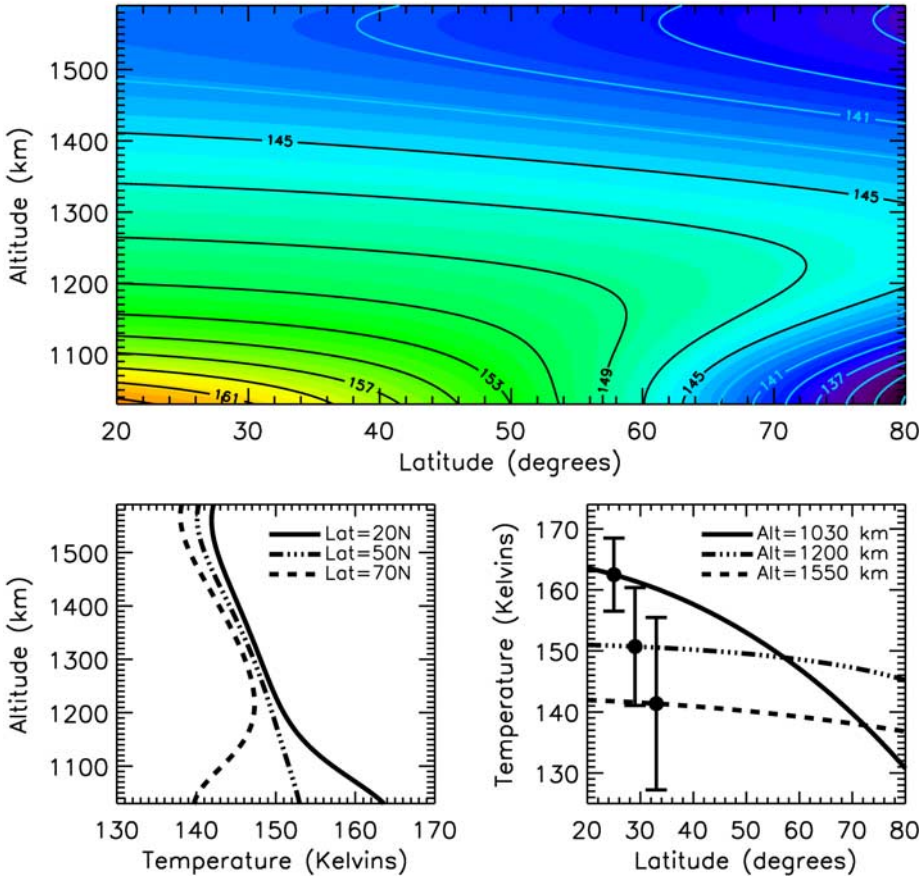

Figure 11. Temperatures in Titan's thermosphere, as inferred from the empirical model atmosphere densities using the method described in the text. (a) Temperatures as a function of latitude and altitude. (b) Vertical temperature profiles at latitudes 20°N (solid), 50°N (dash-dotted) and 70°N (dashed). (c) Temperatures at fixed altitude levels of 1030 km (solid), 1200 km (dash-dotted) and 1590 km (dashed). While the atmosphere is nearly isothermal above around 1200 km altitude, temperatures below 1100 km increase toward the equator. Error bars are also shown and smallest at the lowest heights.

the particular upper boundary condition. An uncertainty of ±15 K in the temperature boundary condition at 1600 km reduces to around ±2 K near 1400 km.

[26] The technique for calculating pressures assumes a vertical column integration in the atmosphere. The inherent difficulty in calculating pressures and temperatures for any single flyby, as is often done, lies in the fact that measurements are carried out along horizontal trajectories along which density changes not only with altitude but also horizontally. As a result, calculation of pressure from densities taken along any single trajectory have an error associated with them, which will affect the inferred temperatures [*Müller-Wodarg et al.*, 2006]. Construction of the empirical model, as described in section 2.2 overcomes this problem. By combining the data from many flybys, we succeed in separating latitudinal from vertical variations, removing a significant source of uncertainty for the derived temperatures.

[27] Temperature error bars are derived using the same procedure as *Müller-Wodarg et al.* [2006]. We derived a series of 10000 pressure and temperature profiles using the technique described above, each time allowing ρ to vary randomly, assuming a Gaussian distribution with a standard deviation equal to the error bar (Figure 7). At each location, this generates 10000 different pressure and temperature values, for which we calculate the standard deviations for the temperature profile.

[28] Figure 11 shows temperatures of Titan's thermosphere, as derived from the empirical model densities. Figure 11a shows temperatures as a function of latitude and altitude. Figure 11b shows vertical temperature profiles at latitudes 20°N (solid), 50°N (dash-triple-dotted) and 70°N (dashed). Figure 11c shows temperatures at fixed altitude levels of 1030 km (solid), 1200 km (dash-triple-dotted) and 1550 km (dashed) with the standard deviations of data superimposed as error bars. Temperatures close to 1000 km vary strongly with latitude, reaching 164 ± 6 K at 20°N and 131 ± 6 K near 80°N. In contrast, Titan's thermosphere appears nearly isothermal above 1200 km with an average temperature of 146 ± 13 K. Exospheric temperature values are in good agreement with the previously derived value of 149 ± 3 K for the TA flyby [*Waite et al.*, 2005; *Yelle et al.*, 2006]. For the latitude range covered by TA (~25–42°N below 1600 km), we obtain an average value of T_{exo} = 145 ± 13 K. The relatively good agreement of these values is due to the fact that TA covered a latitude and altitude range where atmospheric temperatures are virtually constant and latitudinal density variations were

relatively small, below 8%. As a result, the contribution of horizontal variations in TA flyby data was small and derivation of temperatures from the flyby data alone was accurate enough.

[29] In contrast, the T5 flyby covered a latitude range (60°N–76°N) where horizontal density variations reach around 30%, so derivation of temperatures by either fitting vertical density curves to the observations or calculating pressures by downward integration becomes more problematic. For T5, *Müller-Wodarg et al.* [2006] derived an isothermal temperature value of 155 K. The study by *De La Haye et al.* [2007] derived T5 temperatures of 162 K (ingress) and 154 K (egress). When extracting temperatures of Figure 11 along the T5 trajectory we find values to range between 136 and 150 K, clearly lower than the previously derived values, which considered the T5 densities alone. This illustrates the effects of horizontal density variations on derived temperatures. In addition, it shows that we cannot necessarily assume isothermal conditions along any given flyby.

[30] Vertical profiles of temperature derived from the accelerometer measurements by HASI have suggested considerable variability of temperature with altitude on Titan. Large amplitude (10 K) waves around an average temperature value of 170 K dominate the structure between around 800 and 1000 km altitude, followed at higher altitudes by a sharp decrease to around 150 K near 1200 km [*Fulchignoni et al.*, 2005]. While uncertainties remain at those altitudes depending on the choice of boundary conditions in those derivations, the general trend appears remarkably similar to our derived temperatures. Near-equatorial temperatures in our model at latitudes of the HASI measurements range from 172 ± 6 K at 1000 km to 152 ± 10 K at 1200 km. The sharp temperature gradient that we find at low latitudes between 1000 and 1200 km appears consistent with that detected by HASI.

[31] The INMS measurements used in this study were taken during southern hemisphere summer conditions on Titan, the solar declination angle ranging from −23.34° (26 October 2004) to −11.79° (13 June 2007), so solar zenith angles increase toward the northern pole. Solar EUV heating, which forms one of the important energy sources in Titan's thermosphere, will therefore be stronger at the equator than near the northern (winter) pole. Using a General Circulation Model of Titan's thermosphere, *Müller-Wodarg et al.* [2003] calculated global temperatures in Titan's thermosphere, assuming solar EUV heating as the only energy source. Their calculated dayside exospheric temperature decrease at solstice conditions from equator to the winter pole by ∼10 K above 1300 km and less at lower altitudes. As shown in Figure 11, the thermosphere above 1200 km appears to be nearly isothermal, but the uncertainty of ±15 K allows for seasonal variations with latitude consistent with those modeled. The TGCM was unable to obtain the equatorial temperature bulge below ∼1200 km that we see in the INMS observations, so the cause of this bulge is most likely not solar heating.

4. Dynamics of Titan's Thermosphere

[32] The temperature and density structure derived in section 3 can be used to infer dynamics in Titan's thermosphere. The thermal wind equation is used to derive wind speeds from the thermal structure, but this ignores some nonlinear acceleration terms in the momentum equation and molecular viscosity, which have been shown to play an important role in Titan's thermosphere [*Rishbeth et al.*, 1999; *Müller-Wodarg et al.*, 2000]. We therefore use a numerical rather than semianalytical approach to derive the dynamics consistent with the thermal structure.

[33] We use a simplified version of the General Circulation Model by *Müller-Wodarg et al.* [2003] by imposing the thermal structure of Figure 11 and numerically solving the full 3-D momentum equation, but not the energy equation. Our vertical range is 960 km (2.67×10^{-5} Pa) to around 1700 km (5.7×10^{-10} Pa), with isothermal conditions assumed above 1590 km. In order to avoid any horizontal boundary discontinuities, we solve the equations pole-to-pole and assume the same thermal profiles in the northern and southern hemispheres, even though at present,we have no observational constraints from INMS for the southern hemisphere. The full gas continuity equation is solved with molecular and eddy diffusion of the two main gases N_2 and CH_4 as well as optional gas transport by winds. We assume fixed mixing ratios at the lower boundary and optional escape flux for CH_4 at the upper boundary (see section 5). The other details of the model are described by *Müller-Wodarg et al.* [2003]. Because the momentum equation needs to be solved in 3 dimensions, we extend the two-dimensional temperatures of Figure 11 to three dimensions by assuming equal temperatures at all local times for any latitude/height location. While the thermal structure thus varies with altitude and latitude only, the equations are still solved in 3 dimensions. The resulting winds are, of course, local time-independent. We ran the model to steady state, which typically takes 1 Titan rotation for the dynamics and 10 Titan rotations for the composition.

[34] In Figures 12 and 14 we show the three calculated wind components (meridional, zonal, vertical) as a function of altitude and latitude. Figures 12 and 14 show results from simulations for different assumed lower boundary conditions. Figure 12 shows a simulation assuming zero winds at 960 km, whereas Figure 14 shows a case of nonzero winds at the lower boundary. We will discuss these in the following.

[35] When assuming zero winds at 960 km, and hence corotation of the atmosphere at that height with Titan's surface, the dynamics in our simulation are entirely driven by the latitude and altitude gradients of pressure in the atmosphere. We see from Figure 12a that meridional winds are poleward, reaching maximum values of 150 m s^{-1} above 1100 km near 70°N. Above 1100 km meridional winds are virtually constant with altitude, below 1100 km they decrease to zero at 960 km, a result of our boundary condition. The latitudinal pressure gradients, via the large meridional winds, drive a superrotating eastward jet at latitudes poleward of ∼70°N with peak velocity of ∼55 m s^{-1} (Figure 12b). The rotation speed of the thermosphere is around 18 m s^{-1}, so only the region poleward of around 60°N is superrotating.

[36] We find the balance of acceleration terms in the meridional direction to be primarily between advection and the pressure gradients and in the zonal direction to be primarily between advection and curvature terms. The small solid body radius of Titan and its extended atmosphere result in a more curved geometry than on planets like Earth and Venus, and thereby in enhanced curvature

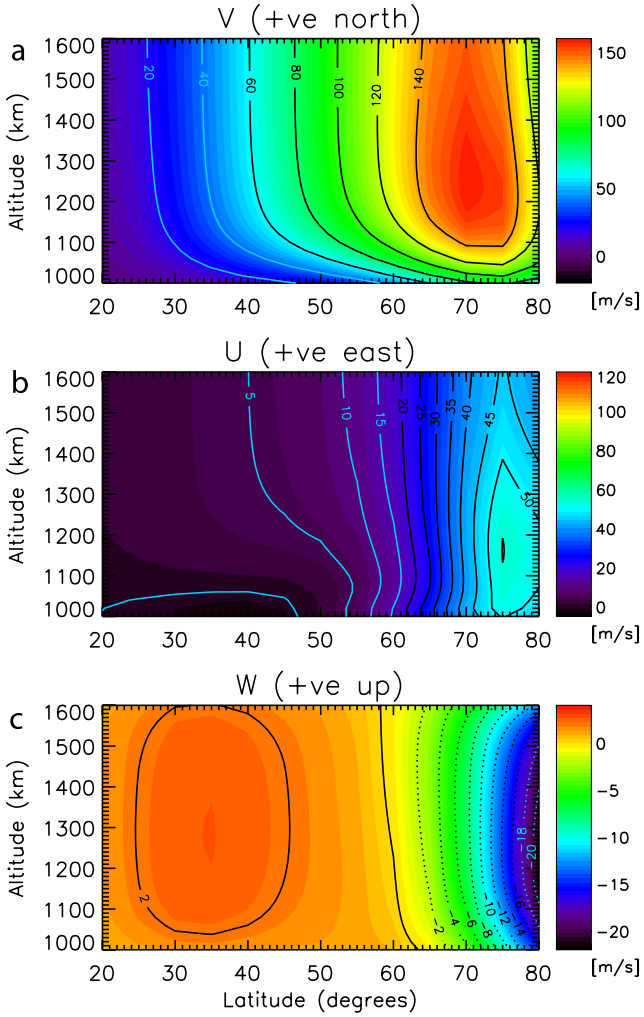

Figure 12. Horizontal and vertical winds in Titan's thermosphere, as derived with our General Circulation Model, assuming the thermal structure of Figure 11. (a) Meridional winds (positive northward), (b) zonal winds (positive eastward), and (c) vertical winds (positive upward). We assume zero winds at the model's lower boundary (960 km).

forces, whereas the slow rotation rate of Titan reduces the importance of the Coriolis term. The key driver of the zonal winds in the absence of any zonal pressure gradients are curvature forces. The strong meridional winds transport angular momentum into the polar regions, limiting the zonal wind growth. Interestingly, this momentum balance differs from that inferred for the solar-driven thermosphere by *Müller-Wodarg et al.* [2000], who found pressure gradients to be balanced primarily by viscosity, a term we found to be less important in our latest simulations. This difference results from the large meridional pressure gradients and associated strong meridional flow which generates the curvature accelerations. The momentum balance in Titan's thermosphere thus ultimately depends on the underlying density structure. Note that the gradient wind balance which is often assumed in the stratosphere of Titan according to our simulations does not apply in its thermosphere.

[37] The divergence of the horizontal winds generates upward winds of ~2 m s^{-1} near equatorial latitudes which turn to subsistence near 65°N, increasing toward the pole with vertical wind speeds of −20 m s^{-1} near 80°N. Seen in the latitude-height plane, therefore, a large circulation cell is formed with upwelling over the equator, poleward flow and subsistence over the pole. A weak equatorward return flow at low altitudes (not seen in Figure 12) closes the flow.

[38] A considerable uncertainty remains whether the base of the thermosphere superrotates, as does Titan's stratosphere [*Hubbard et al.*, 1993; *Flasar et al.*, 2005; *Sicardy et al.*, 2006]. Recent measurements by the Cassini Composite Infrared Spectrometer (CIRS) through nadir and limb sounding of the atmosphere have obtained latitudinal temperature maps from around 5 to 0.005 mbar, from which winds could be inferred via the gradient wind equation up to around 500 km altitude [*Flasar et al.*, 2005; *Achterberg et al.*, 2008]. These studies found zonal jets which peak between around 30 and 60°N near 0.1 mbar with values of up to 190 m s^{-1}, in reasonable agreement with stratospheric winds derived from ground-based observations of two stellar occultations in 2003 [*Sicardy et al.*, 2006]. The CIRS wind maps show a decrease of wind speeds above the 0.1 mbar level, but nothing is known of wind speeds between around 500 and 1000 km altitude on Titan.

[39] Upward propagating waves may considerably affect the momentum balance [*Müller-Wodarg et al.*, 2006; *Strobel*, 2006] and either maintain the atmospheric superrotation up to thermospheric altitudes or suppress it. To assess the influence of possible superrotation on dynamics of the thermosphere, we carried out another simulation with our model where we implemented a profile of superrotating zonal winds at our bottom boundary (near 960 km). We adopted for our lower boundary a zonal wind profile which is based on stratospheric winds inferred by *Achterberg et al.* [2008] from observations by the Cassini Composite Infrared Spectrometer (CIRS) for around 500 km altitude, shown in Figure 13 as a solid line. We applied as our boundary

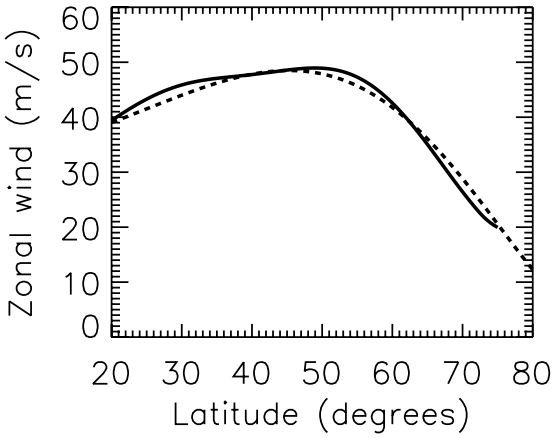

Figure 13. Zonal winds assumed as lower boundary condition in the calculations of Figure 14. The solid line shows stratospheric winds derived from Cassini CIRS thermal maps by *Achterberg et al.* [2008], and the dashed line denotes the winds assumed in our study. The dashed curve is a seventh-degree polynomial fit to the solid line. Values are positive eastward.

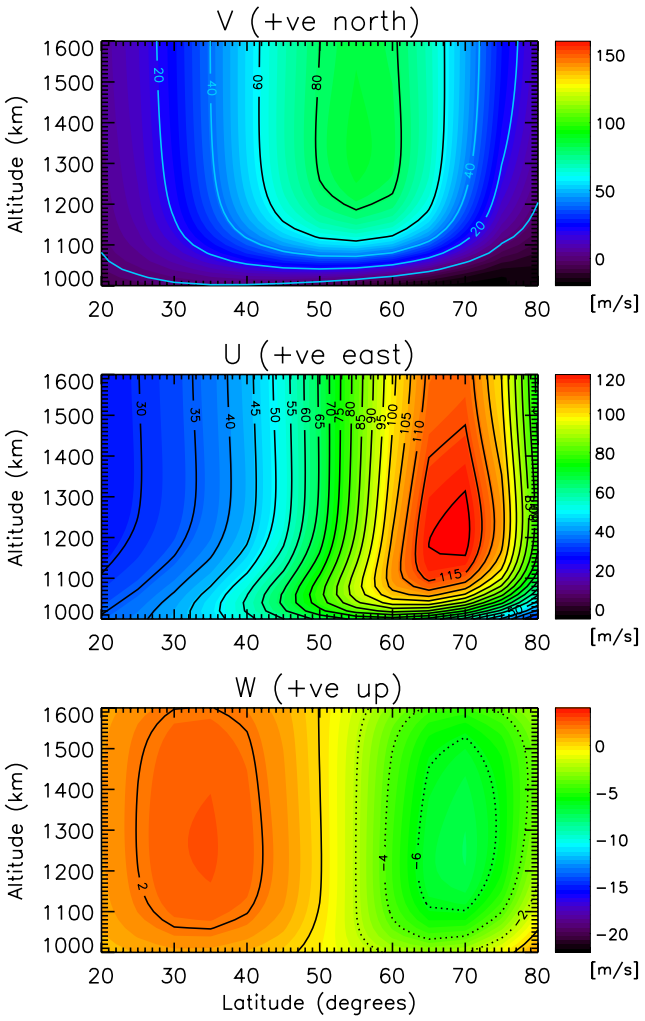

Figure 14. Same as Figure 12 but assuming the stratospheric eastward winds of Figure 13 (dashed line) at the lower boundary (960 km).

condition a seventh-degree polynomial fit to these winds, shown in Figure 13 as the dashed line. As can be seen the velocities are moderate, peaking near 50°N with a value of ~50 m s^{-1}. While zonal winds are likely to change between 500 and 1000 km altitude, our use of this profile is sufficient to assess the sensitivity of thermospheric winds to the lower boundary condition and should be seen only as indicative in the absence of any more accurate constraints from measurements.

[40] Figure 14 shows thermospheric winds calculated with the superrotating lower boundary condition. The circulation differs from the previous calculation of Figure 12 which ignored lower boundary forcing, but some common features are present in both. Peak meridional (poleward) wind speeds occur roughly 15° equatorward of those in the unforced case, near 55°N, reaching around 90 m s^{-1}, or ~70% less. Poleward of 55°N meridional winds gradually decrease to zero. As expected, zonal winds are generally more strongly eastward than in the unforced case and superrotating at all latitudes. The peak zonal jet has moved equatorward by around 10° to ~68°N. The region of strong polar subsistence found in our unforced calculations (Figure 12) has become weaker, with vertical winds of no more than −7 m s^{-1}. The region of strongest subsistence no longer occurs over the pole but near 70°N.

[41] It is of interest to evaluate whether the dynamics in Titan's thermosphere are driven primarily by the temperature gradients or density gradients. The strong meridional winds in our simulations are driven by the latitudinal pressure gradient. From the ideal gas law we may express variations in pressure as a function of variations in density, temperature and mean molecular mass: $\Delta p/p = \Delta\rho/\rho + \Delta T/T - \Delta M/M$. With variations in mean molecular mass being negligible in our context, we evaluated the relative importance of latitudinal density and temperature variations by carrying out two further simulations in which we assumed isothermal conditions at $T = 149$ K and imposed only the horizontal density structure as given by our empirical model. The resulting winds are very similar to those in Figures 12 and 14. This illustrates that the meridional winds are driven primarily by the density gradients and not the temperature gradients, so any uncertainties in our derived thermal structure are to first order irrelevant for the dynamics.

[42] Both circulation patterns shown in Figures 12 and 14 are physically consistent with the imposed density and temperature structures. The numerical calculations illustrate that thermospheric dynamics are not fully constrained by these parameters, but additionally depend on the vertical coupling from below. We have investigated the influence of superrotation from below, but in addition, dynamics may be driven by accelerations due to dissipating waves. Observations by Cassini/Huygens have detected strong waves in Titan's thermosphere [*Fulchignoni et al.*, 2005; *Müller-Wodarg et al.*, 2006] and model calculations have suggested potentially strong wave forcing to occur in the thermosphere [*Müller-Wodarg et al.*, 2006; *Strobel*, 2006]. Since the problem of wave forcing is currently underconstrained by observations, we have not yet attempted to include it in our calculations, but the principle introduces another degree of freedom to dynamics. We will in the following explore additional possible observational constraints on thermospheric dynamics.

5. Latitude Variations of CH_4

[43] Methane is one of the principal gases in Titan's atmosphere and important for the chemistry and energy balance. In Titan's thermosphere CH_4 undergoes photolysis principally by solar Lyα radiation. As shown by *Yelle et al.* [2008], the timescale for Lyα photolysis of CH_4 at the height of strongest absorption (near 850 km) is around 2×10^7 s. The diffusion timescale at that altitude is around 3×10^6 s. Assuming the horizontal and vertical wind velocities derived in section 4, we find transport timescales of up to 1×10^4 s. The numbers illustrate that the photolysis timescale for CH_4 in Titan's thermosphere is significantly larger than dynamical timescales. We may therefore in the context of this study treat CH_4 as chemically inert and expect it to be redistributed in Titan's thermosphere by the winds and diffusion. Inert constituents lighter than the mean molecular mass (~28–25 amu at 1000–1600 km altitude) such as CH_4 will accumulate in regions of subsistence. The response of the CH_4 distribution to transport by

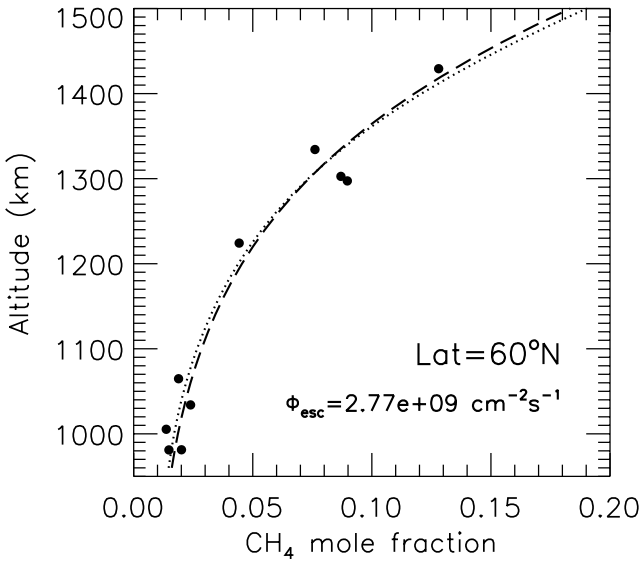

Figure 15. Methane mole fractions in Titan's thermosphere at latitude 60°N. Dots are measurements by the INMS during flybys T5, T16, T18, T19, T21, T27, T28, T30, and T32. The dotted line gives values from the empirical model, while the dashed line represents values from a diffusion model which assumes an eddy coefficient of $K = 3 \times 10^7$ cm^2 s^{-1} and escape flux of $\Phi_{esc} = 2.77 \times 10^9$ cm^{-2} s^{-1} (relative to Titan's surface).

solar driven thermospheric winds on Titan was calculated by *Müller-Wodarg et al.* [2003] using their Thermospheric General Circulation Model. The study showed an accumulation of CH_4 on the nightside and winter hemisphere which resulted from the subsistence of winds there. We can therefore regard CH_4 as a tracer for atmospheric dynamics, so investigating its latitudinal distribution may help constrain thermospheric winds.

[44] Figures 2c, 3c, and 4c show CH_4 mole fractions as a function of latitude. A clear trend is seen with CH_4 abundances increasing toward polar latitudes by up to around 60%. However, it is important to note that these values include the effect of the atmosphere's oblateness, whereby isobar levels are at lower altitudes toward the pole. We find isobaric levels to decrease in altitude by up to around 45 km from equator to pole between 1200 and 1600 km. This implies that along a level of constant altitude we sample regions of lower pressure at polar latitudes, and hence of larger CH_4 abundances due to the diffusive separation. This alone does not constitute a real change in composition. Rather, we need to investigate whether CH_4 mole fractions vary with latitude on an isobar surface.

[45] In order to compensate for the atmospheric oblateness, dotted lines in Figures 2c, 3c, and 4c show the CH_4 mole fractions from the empirical model on levels of constant pressure located close to the plotted altitudes. The mole fractions on a constant pressure level vary less with latitude, by up to around 45%, which is smaller than the error bars. While the implication of this is that the current data set does not allow us to identify a clear increase of CH_4 abundances toward the northern pole on an isobar, there nevertheless remains a suggestive trend that CH_4 accumulates in the northern (winter) polar region in Titan's thermosphere. Such an accumulation of CH_4 would most likely be caused by subsiding winds, in agreement with our calculated dynamics, which showed downwelling at the northern polar latitudes.

[46] In 1-D diffusion models the eddy coefficient is commonly treated as a free parameter which represents small-scale turbulence and larger-scale dynamics not resolved by the model. Previous studies of Titan's atmosphere have derived the eddy coefficient by adjusting its value in order to match particle densities with observations, assuming zero or thermal escape flux at the top boundary. This yielded an eddy coefficient for Titan's thermosphere of a few times 10^8 cm^2 s^{-1}, orders of magnitude larger than that derived for any other planet in our solar system. *Yelle et al.* [2006] point out that the effects of an upper boundary condition of nonzero vertical flux in the continuity equation is similar to that of a large eddy coefficient, and combinations of large eddy coefficient with low escape flux or low eddy coefficient with large escape flux can produce the similar vertical distributions of constituents, introducing an uncertainty in the determination of the true eddy coefficient and escape rates. On Titan, the CH_4 measurements alone cannot solve this ambiguity, and an independent determination of the eddy diffusion coefficient is necessary. Recently, *Yelle et al.* [2008] from analysis of ^{40}Ar data from Cassini/Huygens derived an eddy coefficient in Titan's thermosphere of 3×10^7 cm^2 s^{-1}, an order of magnitude smaller than the value previously assumed, placing the homopause on Titan near the 850 km level.

[47] Figure 15 shows CH_4 mole fractions in Titan's thermosphere at latitude 60°N. The plot shows measurements by the INMS during flybys T5, T16, T18, T19, T21, T27, T28, T30, and T32 alongside values from our empirical model. Also shown in Figure 15 are values from our diffusion model which we ran to steady state assuming an eddy coefficient of $K = 3 \times 10^7$ cm^2 s^{-1} and escape flux of $\Phi_{esc} = 2.77 \times 10^9$ cm^{-2} s^{-1} (relative to Titan's surface). There is very good agreement between the empirical and diffusion models as well as the measurements. Given that no assumptions were made when constructing the empirical model, this good match represents an independent validation of the empirical model. Our diffusion calculations confirm the result by *Yelle et al.* [2008] and show that a large CH_4 escape flux is necessary to reproduce the observed distribution when assuming their eddy coefficient.

[48] Recently, *Strobel* [2008] showed that hydrodynamic escape in Titan's atmosphere could account for such loss rates, while both Jeans escape and nonthermal escape processes are insufficient by orders of magnitude. Hydrodynamic escape on Titan is driven primarily by the energy absorbed through solar EUV absorption and possibly by energy deposited in the thermosphere from the magnetosphere. Thermospheric temperature is largest near the level of peak net EUV heating and decreases toward lower heights, resulting in downward conduction of energy to balance radiative cooling (by HCN rotational lines [cf. *Yelle*, 1991]). Hydrodynamic escape leads to adiabatic cooling above the peak temperature level, leading to a negative temperature gradient with height and upward heat conduction which balances the adiabatic cooling. This signature is clearly present in the derived thermal structure

(Figure 11). We find $dT/dr < 0$ equatorward of around 50°N above 1000 km and poleward of 50°N above 1250 km, supporting the idea of hydrodynamic escape occurring on Titan. No calculations have to date been carried out to characterize the latitude variation of hydrodynamic escape on Titan. The high equatorial temperatures below 1200 km altitude could enhance hydrodynamic escape at those latitude, but the larger solar zenith angles in the northern (winter) hemisphere imply that solar EUV absorption there occurs at higher altitudes, which could increase the proportion of absorbed energy driving escape. It is therefore at this stage unclear how the CH_4 escape rates on Titan change with latitude.

[49] Vertical winds in the thermosphere add another layer of complexity to the problem since they also generate a vertical CH_4 flux in the thermosphere. Our derived vertical winds are weakly upward in the equatorial and low-latitude regions, depleting CH_4 abundances there, while the subsistence at polar latitudes enhances CH_4 abundances. The combined effects of atmospheric dynamics and escape will determine the latitudinal distribution of CH_4, but at present, the problem is still not sufficiently constrained to allow deriving thermospheric winds from the latitudinal variations of CH_4. We intend to further address this problem in future studies.

6. Discussion

[50] Using the combined in situ observations of thermospheric N_2 and CH_4 densities by the INMS during 13 Cassini flybys, we have constructed an empirical model of Titan's thermospheric densities and temperatures. The reasonable agreement between observations and the model allow us to conclude that most features found to date in the INMS along-trajectory densities of N_2 and CH_4 are well explained by latitude and height variations in Titan's thermosphere. The most striking feature we find is the considerable oblateness of Titan's thermosphere. Despite uncertainties in the derived dynamics, we find that this oblateness is likely to drive strongly superrotating prograde jets at high latitudes in the northern (winter) pole. No consistent trend has to date been identified with local time and longitude, which may in part be a result of the zonal winds which can "wash out" zonal variations. However, local time and longitude sampling is sparse to date, and definite conclusions on the variability with these coordinates is not yet possible.

[51] Another important consequence of the horizontal winds is the possibly strong subsistence in the polar regions. This may via adiabatic processes have important effects on the thermal structure there. In fact, simple estimates of adiabatic heating rates which result from the vertical winds in Figure 12 show that these would be comparable to globally integrated solar energy deposition rates. This implies that the winds in Figure 12 cannot be justified in terms of the energetics. Winds in the simulation which includes lower boundary forcing (Figure 12) have less pronounced vertical winds in the polar regions (-5 m s^{-1} instead of -30 m s^{-1}) and still generate substantial adiabatic heating (around 6.5×10^{-10} erg cm^{-3} s^{-1}), but are less problematic from the energetic point of view. This argument would strongly support the notion that winds near 960 km cannot be zero, or else the observed thermal structure cannot be maintained by the resulting vigorous dynamics. We will address this issue in more detail in a future study.

[52] The combined effects of poleward winds and subsistence can accumulate lighter gases (including CH_4 and HCN) in the winter polar region. An enhanced presence of HCN in the winter polar region, if real, would lead to very effective radiative cooling in the region because of emissions in the rotational bands which play a key role in Titan's thermosphere [*Yelle*, 1991]. Recalculating the thermal structure of Titan's thermosphere will be important also at equatorial latitudes, where we found temperatures much larger than at the northern polar latitudes. This will help determine whether the latitudinal thermal structure that we find is a result of latitudinal variations in the net radiative heating rate.

[53] Recent analyses of INMS densities have identified the presence of large atmospheric waves in Titan's thermosphere [*Fulchignoni et al.*, 2005; *Müller-Wodarg et al.*, 2006]. These may through dissipation in the thermosphere deposit significant amounts of momentum there, altering thermospheric winds [*Strobel*, 2006; *Müller-Wodarg et al.*, 2006]. Our calculations of dynamics did not consider waves as a source of momentum. This adds another uncertainty to the wind profiles we calculated from the density and temperature structure since our calculations assumed winds to be driven primarily by pressure gradients. While it is likely that present and future Cassini observations will not be able to further constrain this problem, future studies can explore the possible parameter space for thermospheric winds, taking into account also horizontal variations of composition.

[54] Our calculations in section 4 have shown thermospheric winds to be sensitive to the dynamics of the lower atmosphere. This introduces an uncertainty into our derived horizontal wind profiles that cannot currently be resolved. We found the vertical wind velocities to be particularly sensitive to this lower boundary condition (Figures 12 and 14), which may importantly affect transport of constituents (CH_4, HCN) in the polar regions and adiabatic heating rates there. Our understanding of the high-latitude thermosphere on Titan will thus be particularly sensitive to coupling from below.

[55] In some cases, as discussed in section 2.2.3, the match between our empirical model and observations is poor. Particularly interesting are the differences between T25 and T26 flybys (Figures 8a and 9a). The spacecraft followed almost an identical trajectories through the atmosphere, the solar activity in both cases was similar (see Table 1), and furthermore the position of Titan relative to Saturn was almost identical. Data from the Cassini Magnetometer instrument (MAG) have shown little difference of the overall magnetic field configuration and variability in the vicinity of Titan during these two flybys (C. Bertucci, personal communication, 2007), suggesting that the forcing from Saturn's magnetosphere was comparable during T25 and T26. A more comprehensive analysis of magnetospheric conditions during these flybys, including the characteristics of energetic electrons and ions (measured by the Cassini Plasma Spectrometer, the Radio and Plasma Wave Science experiment and Magnetospheric Imaging Instrument) will be important to determine any differences in magnetospheric forcing

during these flybys. In the absence of evidence for an external forcing mechanism that could cause differences in the atmosphere as observed between T25 and T26, a further possibility is the presence of large-scale waves in the atmosphere which might cause such behavior. Further studies are needed to investigate this.

[56] Our study suggests Titan's thermosphere to be highly variable and dominated by strong dynamics which are accompanied by an oblate shape of the atmosphere at those heights. This picture diverges considerably from the global structure predicted in the pre-Cassini era by general circulation models which considered solar heating alone [*Müller-Wodarg et al.*, 2000]. Much of this results from vertical coupling to lower altitudes, illustrating that the thermosphere of Titan cannot be regarded as an isolated system. Furthermore, we cannot, at present, evaluate the relative importance of various energy sources upon the thermosphere, solar EUV absorption, magnetospheric heating or vertical wave propagation. Further observations in the years to come are expected to enhance our understanding of Titan's atmosphere as a strongly coupled entity.

Appendix A: Data Reduction

[57] In this paper, we examine Cassini Ion Neutral Mass Spectrometer (INMS) data obtained in the Closed Source Neutral (CSN) mode, which is specifically designed for measurements of unreactive neutral species detected in the atmosphere of Titan or other INMS targets [*Waite et al.*, 2004]. The data consists of a sequence of ratios of counting rate versus mass-to-charge ratio, m/z, from $m/z = 1$ to 99 amu per electron charge. In all flybys and for all channels relevant to this work, the INMS samples Titan's upper atmosphere with a time resolution of ~0.9 s, corresponding to a spatial resolution of ~5.4 km along the spacecraft trajectory, for a typical flyby velocity of 6 km s^{-1} relative to Titan.

[58] The INMS data can be analyzed in two ways. For major constituents in Titan's atmosphere (N_2, CH_4), density profiles can be obtained directly from counts in relevant mass channels (usually the channels of main peaks in their cracking patterns) as a function of altitude [*Yelle et al.*, 2006]. In contrast, analysis of minor constituents (C_2H_2, C_2H_4, etc.) requires careful modeling of mass cracking patterns in the observed full mass spectrum. The full mass spectrum is usually obtained by integrating the counts in all channels over a particular altitude range. The spectral analysis used to determine minor species densities is described elsewhere [*Waite et al.*, 2005; J. Cui et al., Analysis of neutral mass spectra from Cassini/INMS observations of Titan, submitted to *Journal of Geophysical Research*, 2008]. Here, we present the methodology used in determination of major species densities.

[59] The INMS flight unit (FU) was calibrated prior to launch with a small number of reference gases, including N_2 and CH_4. In our analysis, these sensitivities are used to infer number densities from count rates. However, the N_2 and CH_4 gases are mixtures of their isotopes and isotopic ratios may differ in the atmosphere of Titan and Earth and may vary with altitude. It is therefore necessary to determine sensitivities for N_2, $^{14}N^{15}N$, CH_4 and $^{13}CH_4$ separately, allowing for the possibility of different isotope ratios on Titan. Details of the procedure are described by Cui et al. (submitted manuscript, 2008). Here, we concentrate exclusively on the main isotopes.

[60] The INMS has both a high-gain counter ($C^{(1)}$) and a low-gain counter ($C^{(2)}$). The $C^{(1)}$ counts in channels $m/z = 28$, 29, and 16 are used to determine the densities of N_2, $^{15}N^{14}N$, CH_4 and $^{13}CH_4$ when possible. However, the $C^{(1)}$ counter for channel 28 becomes saturated below ~1300 km in all flybys and is likely to be saturated for channels 14, 15, 16, and 29 at low-altitude passes. When this happens we determine densities either from $C^{(2)}$ counts of the main peak channel or alternatively from $C^{(1)}$ counts in other channels where the cracking pattern of the species shows sufficiently large counts. For the former case, the $C^{(2)}/C^{(1)}$ conversion factor has to be determined. For the latter case, calibration between density values determined from different channels is required to ensure consistency. This may be associated with the fact that the dissociative ionization of a molecule imparts the dissociation fragments with excess kinetic energy which may affect the way that the fragment ions are transmitted through the ion optics of the INMS. In all cases, we assume that the densities inferred from the main peak channel of a given species are correct, to which we calibrate densities determined from other channels.

[61] The cracking pattern of N_2 has peaks at $m/z = 28$ and 14, produced by N_2^+ and N^+ ions. To derive N_2 densities, we use $C^{(2)}$ counts in channel 28 below 1100 km (where $C^{(1)}$ counts in channels 14 and 28 are both saturated), we use $C^{(1)}$ counts in channel 28 above 1300 km where it is not saturated, and we use $C^{(1)}$ counts in channel 14 between 1100 and 1300 km (where $C^{(1)}$ counts are saturated in channel 28 but not in channel 14). The switch to counts in channel 14 for the density determination at intermediate altitudes is based on the consideration that $C^{(1)}$ counts in channel 14 are always much higher than $C^{(2)}$ counts in channel 28 and therefore have a higher signal-to-noise ratio.

[62] For calibration of N_2 densities determined from different channels, we calculate the ratio of the N_2 density determined from channel 28 to that determined from channel 14 between 1300 and 1600 km for each flyby. The lower boundary is selected to ensure that $C^{(1)}$ counts are not affected by saturation. Counts of channel 14 are contributed by N_2, CH_4, and $^{14}N^{15}N$, and the contributions from CH_4 and $^{14}N^{15}N$ have to be subtracted for an accurate determination of N_2 densities from this channel. Here CH_4 densities are calculated from $C^{(1)}$ counts in channel 16, and $^{14}N^{15}N$ densities from $C^{(1)}$ counts in channel 29. On the basis of the above procedure, we obtain a N_2 scaling factor for channel 14, which varies by 5% from flyby to flyby and has an average value of 0.79.

[63] The $C^{(2)}$-$C^{(1)}$ conversion factor for channel 28 can in principle be determined by taking the average ratio of $C^{(1)}$ counts to $C^{(2)}$ counts at the same altitudes where the $C^{(1)}$ counter is not saturated for channel 28. However, $C^{(2)}$ counts are very low in regions where $C^{(1)}$ counts are not saturated, making it difficult to estimate the conversion factor from counts in channel 28 directly. Instead, we use the procedure described above to determine N_2 densities above 1100 km from $C^{(1)}$ counts in channel 14, and then predict the corresponding $C^{(1)}$ counts in channel 28. Here the N_2 scaling factor for channel 14 as determined above has been used for calibration. With the predicted C^1 counts and measured $C^{(2)}$ counts in channel 28, the $C^{(2)}$-$C^{(1)}$ conversion factor can be

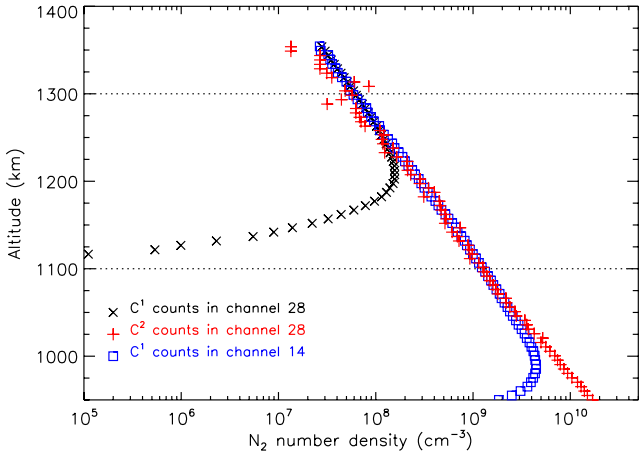

Figure A1. The N_2 density profile for inbound measurements during the T16 flyby (22 July 2006). Above 1300 km, N_2 densities are determined from $C(^1)$ counts in channel 28 (black crosses); between 1100 and 1300 km, densities are determined from $C(^1)$ counts in channel 14 (blue squares) and below 1100 km, densities determined from $C(^2)$ counts in channel 28 (red pluses). Densities from both $C(^1)$ counts in channel 14 and $C(^2)$ counts in channel 28 have been calibrated to those from C1 counts in channel 28 (see Appendix A).

calculated accurately, assuming that it is a constant for each flyby. This conversion factor varies by 6% from flyby to flyby, with an average value of 5470.

[64] As an example, we show in Figure A1 the altitude profile of N_2 densities calculated from $C^{(1)}$ (black crosses) and $C^{(2)}$ (blue/black squares) counts of channel 28, as well as $C^{(1)}$ counts (red/gray plus signs) of channel 14, for the inbound measurements taken at the T16 flyby (22 July 2006). The dotted lines mark where the determination of N_2 densities switch from one algorithm to another.

[65] The cracking pattern of CH_4 has peaks at m/z = 12, 13, 14, 15, and 16, produced by CH_x^+ ions where x ranges from 0 to 4. In most cases, the CH_4 densities can be determined accurately from $C^{(1)}$ counts in channel 16. The contribution from $^{13}CH_4$ to m/z = 16 has to be subtracted, with $^{13}CH_4$ densities easily obtained from $C^{(1)}$ counts in m/z = 17. However, the $C^{(1)}$ counter of channel 16 becomes saturated below ~1100 km, and the CH_4 densities have to be calculated differently in that region. $C^{(2)}$ counts in channel 16 cannot be used since they are too noisy. Since $C^{(1)}$ counts in channels 14 and 15 may also be saturated at low altitudes and have large contributions from N_2 and $^{15}N^{14}N$, we use $C^{(1)}$ counts in channels 12 and 13 to determine CH_4 densities below 1100 km. Counts in channels 12 and 13 are also contributed by C_2H_2 and C_2H_4 and for channel 13, $^{13}CH_4$ provides an additional contribution. All these minor contributions have to be subtracted. While $^{13}CH_4$ densities are easily obtained from $C^{(1)}$ counts in channel 17, an estimate of C_2H_2 and C_2H_4 is uncertain since these two species have complex cracking patterns. Counts in channels 24, 25 and 26 can in principle be used to constrain densities of C_2H_2 and C_2H_4, with minor contributions from other hydrocarbons (C_2H_6, C_3H_8, C_6H_6, etc.) ignored. However, the cracking patterns of C_2H_2 and C_2H_4 are very similar for channels 24, 25 and 26, in the sense that the branching ratios of C_2H_2 are approximately a factor of 3 higher than those of C_2H_4 for all these channels but the relative signals are the same. This implies that counts in these channels can only be used to constrain the linear combination of C_2H_2 and C_2H_4 densities, in the form of $n_{C2H2} + \frac{1}{3}n_{C2H4}$.

[66] Assuming pure C_2H_2, counts in each of the channels 24, 25, and 26 give an independent estimate of the C_2H_2 densities. At any given altitude, the mean value is adopted and used to calculate the contribution from C_2H_2 to channels 12 and 13. With contributions from C_2H_2 and $^{13}CH_4$ subtracted, the remaining counts in these two channels can then be used to determine CH_4 densities. In the alternative extreme case in which we assume pure C_2H_4, we obtain similar densities of CH_4, consistent with the results for the pure C_2H_2 case within 1-sigma uncertainties. This similarity is mainly due to the fact that the contributions from C_2H_2 and C_2H_4 to channels 12 and 13 are small.

[67] As for N_2, CH_4 densities determined from different channels have to be corrected to ensure consistency among densities in different altitude ranges. The scaling factors for CH_4 for channels 12 and 13 are obtained similarly to the adjustments to N_2 for channel 14 as described above. This results in a smooth CH_4 density profile for each flyby, which does not show any discontinuity at 1100 km where the density determination switches from channel 16 to channels 12 and 13. In our analysis, the average value of CH_4 density determined from channels 12 and 13 is used at any given altitude below 1100 km.N_2 and CH_4 density profiles are extracted from INMS data with the procedures described above, for both inbound and outbound measurements. The outbound measurements of some minor species are strongly affected by absorption from the walls of the instrument [*Vuitton et al.*, 2007]. However, this is not an issue for N_2 and CH_4 at lower altitudes. A comparison between the inbound and outbound density profiles averaged over all flybys to smooth out horizontal variations shows that the inbound and outbound average profiles are nearly identical below ~1800 km for both N_2 and CH_4, implying that the wall chemistry effect is not a concern for this study.

[68] **Acknowledgments.** I.M.-W. is funded by a University Research Fellowship of the British Royal Society. R.V.Y. and J.C. have been supported by NASA grant NAG5-12699 to the University of Arizona. J.H.W. is funded by NASA and the Jet Propulsion Laboratory contract 1283095 with Southwest Research Institute. We wish to thank our referees Darrell Strobel and Jared Bell for their valuable comments on this manuscript.

References

Achterberg, R. K., B. J. Conrath, P. J. Gierasch, F. M. Flasar, and C. A. Nixon (2008), Titan's middle-atmospheric temperatures and dynamics observed by the Cassini Composite Infrared Spectrometer, *Icarus*, *194*, 263–277, doi:10.1016/j.icarus.2007.09.029.

Broadfoot, A. L., et al. (1981), Extreme ultraviolet observations from Voyager 1 encounter with Saturn, *Science*, *212*, 206–211.

De La Haye, V., et al. (2007), Cassini INMS data in Titan's upper atmosphere and exosphere: Observations of a suprathermal corona, *J. Geophys. Res.*, *112*, A07309, doi:10.1029/2006JA012222.

Flasar, F. M., et al. (2005), Titan's atmospheric temperatures, winds, and composition, *Science*, *308*, 975–978, doi:10.1126/science.1111150.

Fulchignoni, M., et al. (2005), In situ measurements of the physical characteristics of Titan's environment, *Nature*, *438*, 785–791, doi:10.1038/nature04314.

Hedin, A. E., H. B. Niemann, W. T. Kasprzak, and A. Seiff (1983), Global empirical model of the Venus thermosphere, *J. Geophys. Res.*, *88*, 73–83.

Hubbard, W. B., et al. (1993), The occultation of 28 SGR by Titan, *Astron. Astrophys.*, *269*, 541–563.

Müller-Wodarg, I. C. F., R. V. Yelle, M. J. Mendillo, L. A. Young, and A. D. Aylward (2000), The thermosphere of Titan simulated by a global three-dimensional time-dependent model, *J. Geophys. Res.*, *105*, 20,833–20,856.

Müller-Wodarg, I. C. F., R. V. Yelle, M. J. Mendillo, and A. D. Aylward (2003), On the global distribution of neutral gases in Titan's upper atmosphere and its effect on the thermal structure, *J. Geophys. Res.*, *108*(A12), 1453, doi:10.1029/2003JA010054.

Müller-Wodarg, I. C. F., R. V. Yelle, N. Borggren, and J. H. Waite (2006), Waves and horizontal structures in Titan's thermosphere, *J. Geophys. Res.*, *111*, A12315, doi:10.1029/2006JA011961.

Rishbeth, H., R. V. Yelle, and M. Mendillo (1999), Dynamics of Titan's thermosphere, *Planet. Space Sci.*, *48*, 51–58.

Shemansky, D. E., A. I. F. Stewart, R. A. West, L. W. Esposito, J. T. Hallett, and X. Liu (2005), The Cassini UVIS Stellar Probe of the Titan Atmosphere, *Science*, *308*, 978–982, doi:10.1126/science.1111790.

Sicardy, B., et al. (2006), The two Titan stellar occultations of 14 November 2003, *J. Geophys. Res.*, *111*, E11S91, doi:10.1029/2005JE002624.

Smith, G. R., D. F. Strobel, A. L. Broadfoot, B. R. Sandel, D. E. Shemansky, and J. B. Holberg (1982), Titan's upper atmosphere: Composition and temperature from the EUV solar occultation results, *J. Geophys. Res.*, *87*, 1351–1359.

Strobel, D. F. (2006), Gravitational tidal waves in Titan's upper atmosphere, *Icarus*, *182*, 251–258, doi:10.1016/j.icarus.2005.12.015.

Strobel, D. F. (2008), Titan's hydrodynamically escaping atmosphere, *Icarus*, *193*(2), 588–594, doi:10.1016/j.icarus.2007.08.014.

Vervack, R. J., B. R. Sandel, and D. F. Strobel (2004), New perspectives on Titan's upper atmosphere from a reanalysis of the Voyager 1 UVS solar occultations, *Icarus*, *170*, 91–112, doi:10.1016/j.icarus.2004.03.005.

Vuitton, V., R. V. Yelle, and M. J. McEwan (2007), Ion chemistry and N-containing molecules in Titan's upper atmosphere, *Icarus*, *191*, 722–742, doi:10.1016/j.icarus.2007.06.023.

Waite, J. H., et al. (2004), The Cassini Ion and Neutral Mass Spectrometer (INMS) investigation, *Space Sci. Rev.*, *114*, 113–231, doi:10.1007/s11214-004-1408-2.

Waite, J. H., et al. (2005), Ion Neutral Mass Spectrometer results from the first flyby of Titan, *Science*, *308*, 982–986, doi:10.1126/science.1110652.

Yelle, R. V. (1991), Non-LTE models of Titan's upper atmosphere, *Astrophys. J.*, *383*, 380–400.

Yelle, R. V., N. Borggren, V. de La Haye, W. T. Kasprzak, H. B. Niemann, I. Müller-Wodarg, and J. H. Waite (2006), The vertical structure of Titan's upper atmosphere from Cassini Ion Neutral Mass Spectrometer measurements, *Icarus*, *182*, 567–576, doi:10.1016/j.icarus.2005.10.029.

Yelle, R. V., J. Cui, and I. C. F. Müller-Wodarg (2008), Methane escape from Titan's atmosphere, *J. Geophys. Res.*, *113*, E10003, doi:10.1029/2007JE003031.

J. Cui and R. V. Yelle, Lunar and Planetary Laboratory, University of Arizona, 1629 E. University Boulevard, Tucson, AZ 85721, USA. (jcui@lpl.arizona.edu; yelle@lpl.arizona.edu)

I. C. F. Müller-Wodarg, Space and Atmospheric Physics Group, Imperial College London, Prince Consort Road, London SW7 2BW, UK. (i.mueller-wodarg@imperial.ac.uk)

J. H. Waite, Southwest Research Institute, 6220 Culebra, San Antonio, TX 78228-0510, USA. (hwaite@swri.edu)